Finite Element Model of Polar Growth in Pollen Tubes [C][W]

Pierre Fayant,[a] Orlando Girlanda,[a,1] Youssef Chebli,[b] Carl-Éric Aubin,[a] Isabelle Villemure,[a] and Anja Geitmann[b,2]

[a] École Polytechnique de Montréal, Case Postale 6079, Succursale Centre-Ville, Montreal, Quebec H3C 3A7, Canada
[b] Institut de Recherche en Biologie Végétale, Département de Sciences Biologiques, Université de Montréal, Montreal, Quebec, H1X 2B2, Canada

Cellular protuberance formation in walled cells requires the local deformation of the wall and its polar expansion. In many cells, protuberance elongation proceeds by tip growth, a growth mechanism shared by pollen tubes, root hairs, and fungal hyphae. We established a biomechanical model of tip growth in walled cells using the finite element technique. We aimed to identify the requirements for spatial distribution of mechanical properties in the cell wall that would allow the generation of cellular shapes that agree with experimental observations. We based our structural model on the parameterized description of a tip-growing cell that allows the manipulation of cell size, shape, cell wall thickness, and local mechanical properties. The mechanical load was applied in the form of hydrostatic pressure. We used two validation methods to compare different simulations based on cellular shape and the displacement of surface markers. We compared the resulting optimal distribution of cell mechanical properties with the spatial distribution of biochemical cell wall components in pollen tubes and found remarkable agreement between the gradient in mechanical properties and the distribution of deesterified pectin. Use of the finite element method for the modeling of nonuniform growth events in walled cells opens future perspectives for its application to complex cellular morphogenesis in plants.

INTRODUCTION

Cellular growth is a fundamental process during plant development. It shapes cellular morphology, affects cell functioning, and ultimately determines the plant phenotype. During expansive plant cell growth, the cell wall needs to be mechanically stretched, which leads to its thinning, and, vital to cell survival, new material needs to be incorporated into the existing wall to prevent fatal rupture. Growth of plant cells is thus a complex interaction between the internal turgor-generated hydrostatic pressure, which drives this process, and the surrounding cell wall, which regulates its temporal and spatial dynamics (Cosgrove, 2005; Schopfer, 2006; Geitmann and Ortega, 2009). Understanding the biomechanical underpinnings of cellular growth processes will help us to focus our attention on those cellular mechanisms and molecular pathways that govern relevant physical players involved in plant development.

Cell morphogenesis in plants comes in a wide spectrum, with diffuse growth at one end of the continuum and the highly polarized phenomenon of tip or polar growth at the other end (Wasteneys and Galway, 2003). Combinations of these two processes lead to the generatio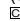n of complex plant cell geome-tries, such as those of star-shaped astrosclereids and jigsaw puzzle–shaped leaf epidermis cells (Mathur, 2004; Smith and Oppenheimer, 2005; Mathur, 2006; Geitmann and Ortega, 2009). Since the hydrostatic pressure driving cell wall stretching is a nonvectorial force, the regulation of the final cell shape lies in the mechanical properties of the cell wall. The diffuse increase in overall cell size, typical for example for root epidermis cells, is known to be regulated by the arrangement of the cellulose microfibrils (Baskin, 2005). Attempts to simulate this diffuse type of expansive growth date back to the first analytical model for cell expansion by Lockhart (1965). The constitutive equations describing growth behavior have been modified and adapted to various experimental situations (Geitmann and Ortega, 2009), and efforts to mathematically account for the fiber-reinforced composite behavior of the cell wall are underway (Dyson and Jensen, 2010).
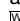
The generation of complex cellular geometries, on the other hand, represents a major challenge for analytical modeling. The reasons for the complexity of cells such as those composing the leaf epidermis are their geometry and their material properties, whose mathematical representation requires numerical modeling approaches. In engineering, the method commonly used to predict the mechanical behavior of complex structures is based on finite element (FE) modeling techniques. For this approach, the structural system is divided into discrete areas, the elements, which are connected by characteristic key points (generally located at their corners), or nodes. The quantities of interest, stresses, strains, and displacements, are evaluated at the nodes connecting different elements. The FE technique produces approximate solutions to complex problems and by doing this allows for the calculation of the behavior of structures with complicated geometry and material properties. FE modeling has

been used recently to model the elastic, temporary deformation of plant tissues and cells under the application of temporary external loads (Bolduc et al., 2006; Wang et al., 2006; Hamant et al., 2008), but its utility for modeling the mechanics of cellular growth processes remains unexplored. Our objective was to use FE modeling to represent a spatially confined cellular growth process in plants to demonstrate the potential of this approach for plant developmental research.

The experimental system chosen for our modeling approach is tip growth. Tip growth is a widespread mode of cellular morphogenesis found not only in plants (root hairs and pollen tubes), but also in animals (neurons), fungi (hyphae and budding yeasts), alga (rhizoids), and prokaryotes (streptomycetes). The defining feature of this growth process is the spatial confinement of surface expansion to the extremity of the cell. Consequently, all the key processes that regulate morphogenesis can be observed concomitantly in a small cellular region. The resulting structure is a tubular protrusion capped by a hemisphere or hemispheroid-shaped dome.

Among the modes of growth leading to complex geometry, tip growth has the advantage of having a simple radial symmetry. Furthermore, the growth process displays temporal self-similarity, which means that the shape profile of the apical region of the cell stays largely constant in time and simply moves forward along the longitudinal axis of the cell (Goriely and Tabor, 2003a). These features facilitate the establishment of quantitative validation strategies for a theoretical model. Furthermore, tip growth has attracted a number of earlier modeling attempts (Bartnicki-Garcia et al., 2000; Bartnicki-Garcia, 2002; Goriely and Tabor, 2003a, 2003b; Dumais et al., 2004, 2006; Goriely and Tabor, 2008; Kroeger et al., 2008; Campàs and Mahadevan, 2009), all of which have their merits and limitations. Most importantly in this context, all of these models are essentially limited in their application to the simple, radial symmetry of the tip-growing cell. Their adaptation to more complex geometries is not or not readily possible. FE techniques on the other hand offer this flexibility.

Tip growth is easily affected through mutation and enzymatic or pharmacological action. This interference often results in a swelling (Malhó et al., 1995; Kost et al., 1999; Parre and Geitmann, 2005a; Klahre et al., 2006; Klahre and Kost, 2006; Aouar et al., 2010; Hwang et al., 2010) or tapering (Klahre and Kost, 2006) of the tubular cell or, in extreme cases, in the arrest of growth or bursting. A phenomenon such as apical swelling is generally claimed to be the result of a depolarization of the growth process, but how intracellular events are translated into a change of cellular morphology has not been examined in detail. A crucial question we wanted to address with our theoretical model concerns the nature of the changes to the cell wall mechanical properties that are implied in the generation of phenotypes that differ from the perfectly self-similar elongation pattern typical of the undisturbed cell. Geometrical and biophysical considerations dictate that the cell wall of the growing apex in tip-growing cells must have a higher degree of extensibility than its cylindrical portion to direct cellular expansion to the apex (Geitmann and Steer, 2006). Using an FE model, we wanted to find out exactly how this mechanical gradient must be shaped to generate a self-similar growth pattern for a given initial shape and how changes

in this gradient affect the shape of the growing tube. To demonstrate the relevance of our theoretical approach, we compared the results of the simulations with the spatial distribution of the biochemical components of the cell wall and with the growth behavior of pollen tubes, a widely used cellular model for tip growth (Hepler et al., 2001; Geitmann and Steer, 2006; Chebli and Geitmann, 2007).

Construction of the FE Model and Validation Methods

We used the FE method (ANSYS 11.0 finite element package) to generate a FE mesh structure that represents the geometry of a typical tip-growing cell and to model the deformation of the cell wall resulting from a hydrostatic pressure load. We constructed a shell based on a parameterized geometrical description that corresponds to the typical shape of the apical region of a pollen tube. We subdivided the structure in several ring-shaped domains along the longitudinal axis to be able to assign different mechanical properties to the different regions of the tube. Basic information that is required to develop an FE model includes geometry, mechanical properties, loading parameters, and boundary conditions, as detailed below. To identify the combination of mechanical properties resulting in self-similar growth, we developed a procedure to quantitatively determine the similarity of the simulation results with experimental data on cell shape and growth. These procedures served to validate our model.

Geometry and Meshing

Pollen tubes are cylindrical cells capped by an apex shaped like a half prolate spheroid. Using bright-field micrographs, we determined that the shape of pollen tubes is well described by a relationship of $r_L = 1.5 \times r_T$, with r_T being the radius of the tube and thus the short radii of the prolate spheroid and r_L being the long radius of the spheroid (Figure 1). In this model, we used $r_T = 6$ μm unless noted otherwise. The structure of the tube was thus defined by the radius of the cylinder (r_T), the long radius of the apical spheroid (r_L), and the thickness (t) of the shell representing the cell wall. For this model, the thickness of the shell was assumed to be constant at 50 nm unless noted otherwise. The pollen tube shank and its apical region were meshed using user-defined thickness and four-node shell type elements with 6 degrees of freedom at each node (SHELL181) (Figures 2A to 2C).

To assign different mechanical properties to the shell elements depending on their position on the tube surface, the structure was divided along the longitudinal axis into seven domains, six of which were located in the spheroid portion and the seventh being formed by the cylindrical shank (Figure 2D). The meridional lengths of domains 1 to 6 were defined by key points, which are anchor points for geometry and meshing. The position of each key point was defined by the angle θ_i that a connecting line between the key point and center of the spheroid formed with the previous domain. These angles could be varied to modulate the shape of the gradient in cell wall mechanical properties. For the purpose of obtaining a self-similar growth pattern, we focused on the gradient of mechanical properties in the apical dome of the cell. Therefore, for the sets of simulations analyzed here, the sum of angles 1 through 6 was always adjusted to be 90°.
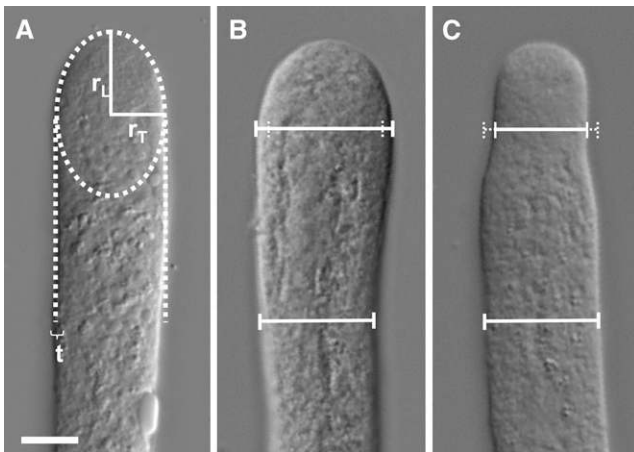
Figure 1. Differential Interference Contrast Micrographs of in Vitro–Growing Lily Pollen Tubes.

(A) Normally growing tube. The geometry of the tube can be described with a cylinder of radius r_T capped by a half prolate spheroid with short radii r_T and a long radius r_L. The dotted line describes the two-dimensional profile of the shape defined by an ellipse and a rectangle.
(B) Tube showing a swelling apical region. Solid lines describe the diameter of the tube at different locations. Dotted line indicates the length of the distal diameter for comparison.
(C) Tube showing a tapering apical region. Solid lines describe the diameter of the tube at different locations. Dotted line indicates the length of the distal diameter for comparison.
Bar = 10 μm

Domains 2 to 7 were meshed using a mapped mesh consisting of quadrilateral elements arranged in rows. However, domain 1 is triangular in shape. To use the same type of element (four-node shell elements), some of the quadrilateral elements had to be rotated, which is done by a free mesh generator (Figure 2C). Mesh density was determined through convergence testing. This means that simulations with structures having denser meshes were performed, but no significant difference in the results was observed.

Mechanical Properties

The distribution of the material properties in the cell wall was chosen to correspond to the qualitative information that is available on the distribution of cell wall material in pollen tubes (Li et al., 1994; Parre and Geitmann, 2005a, 2005b; Aouar et al., 2010). The pole of the cell consists mainly of pectin, an isotropic material. Although cellulose is present, it is randomly oriented (Sassen, 1964). We therefore used an isotropic material model to describe the pole region (domain 1; Figure 2D). In the shank, cellulose microfibrils display a preferential orientation oblique to the growth axis (O'Kelley and Carr, 1954; Sassen, 1964; Aouar et al., 2010). It is unknown exactly how microfibrils are oriented in the regions of the apical dome located between pole and shank. Therefore, any potential anisotropy in the plane of the wall, caused by preferential orientation of cellulose microfibrils, was considered using an orthotropic material model for domains 2 through 6.

In the model, the elastic moduli of shell elements lying within domains 1 (pole) and 7 (shank) are directly user defined. In domains 2 through 6, the values of the longitudinal elastic moduli are linked by a factor m_L. The transversal value of the elastic modulus is obtained by multiplying the longitudinal elastic modulus by a factor m_T.

The increase of the longitudinal elastic modulus from one domain to the next is represented by the following rule:

$$E_{Li} = m_L \times E_{Li-1},$$

where E_{Li} is the longitudinal Young's modulus in domain i. The Young's modulus is a measure of stiffness of an elastic material. Higher values indicate a lower degree of deformability. Modulating parameter m_L changes the steepness in the mechanical gradient along the longitudinal axis.

The transversal elastic modulus E_{Ti} within each domain I is then calculated by:

$$E_{Ti} = m_T \times E_{Li}.$$

The parameter m_T reflects the degree of anisotropy of the material in the plane of the shell. The elastic modulus in normal direction E_{Zi} was set to always be identical to E_{Ti}.

Given that at the pole, the cell wall consists almost exclusively of pectins, we used a value of 12.5 MPa for the elastic modulus of domain 1 (Chanliaud and Gidley, 1999). The longitudinal and the transversal elastic moduli of the shank (domain 7) were chosen to be 4000 MPa to represent its large stiffness compared with the apical region of the tube. Preliminary simulations had shown that lower values would result in an increase in the tube diameter in the shank region. This increase would be incompatible with self-similarity; therefore, no further tests were performed with lower values for domain 7. The Poisson ratio of 0.3 was kept identical for all domains (Chanliaud et al., 2002). This ratio indicates the contraction (elongation) of a stretched (compressed) material in the direction perpendicular to the applied tension (compression).

Boundary Conditions

To reduce calculation time, we exploited the radial symmetry of the pollen tube and modeled only a quarter of the cylindrical structure, unless mentioned otherwise (Figure 2A). At the axisymmetric borders, radial and longitudinal translations were fixed. Vertical translation was prevented by fixing the base of the shank.

Loading Parameters

The turgor pressure within the cell was represented by an internal hydrostatic pressure of 0.2 MPa, unless noted otherwise, based on the values measured in *Lilium longiflorum* pollen tubes (Benkert et al., 1997).

Simulation of Pollen Tube Growth

Growth of the cell was simulated by an iterative series of loading cycles. Load was applied, and the resulting deformed structure represented the starting geometry for the subsequent loading cycle. To account for the fact that continuous deposition of new cell wall material takes place during tip elongation, the structure was remeshed after each loading cycle (Figures 2B and 2E). This
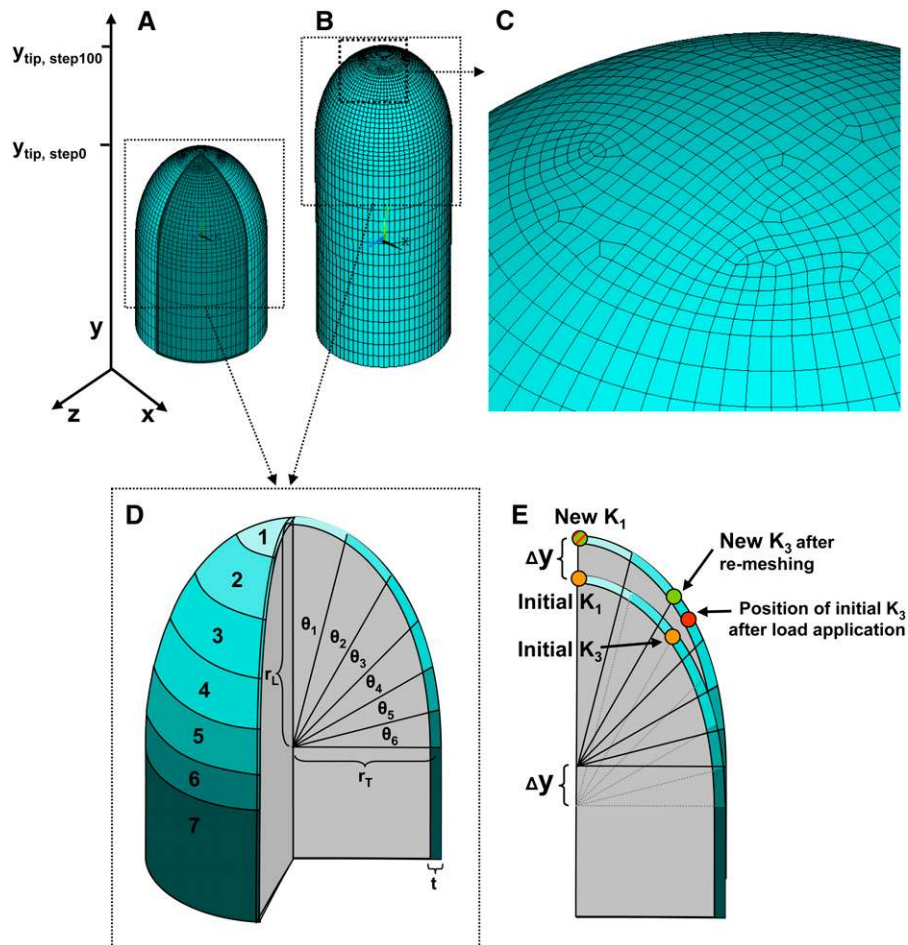
Figure 2. FE Structure of a Tip-Growing Cell.

Initial structure **(A)** and structure after 50 load cycles (**[B]** and **[C]**) in the case of self-similar elongation. The figures show the full 360° structure and the 90° structure marked in darker color in **(A)**. For most calculations, only the 90° structure is used to exploit radial geometry. The apical region of the cell wall is divided into six ring-shaped surface domains defined by the angles θ_1 through θ_6, originating from the center of the prolate spheroid **(D)**. Because of its different geometry, domain 1 is meshed using a different method than domains 2 through 7. This resulted in irregularly arranged shell elements in the pole region **(C)**. The shape of the pollen tube is defined by the short radii r_T and the long radius r_L of the half prolate spheroid and the thickness t of the shell elements representing the cell wall. Deformation resulting from load application causes the displacement of key points defining surface regions **(E)**. These are redefined after remeshing based on the domain angles θ_i **(D)**.

implied that to ensure constant mesh density, nodes were added to accommodate for the increased length of the structure. Cell wall thickness was set back to the original value to mimic the deposition of additional cell wall material by exocytosis. Furthermore, to reflect the continuous maturation of the cell wall upon its displacement toward the cylindrical shank, the ring-shaped cell wall regions were redefined after each loading cycle based on the angles that were maintained constant (Figure 2E). This implied the redefinition of the key points defining the surface domains.

Validation of the Model

One of the objectives of the study was to build a model that was capable of representing perfectly self-similar growth. To assess

the quality of the different simulation runs, we devised two quantitative validation methods that allowed us to determine how closely the model behaved to the real cell.

Degree of Self-Similarity

Tip-growing cells grow in an approximately self-similar manner when undisturbed. To determine the degree of self-similarity resulting from the FE simulations, the shape of the structure after 100 loading cycles was compared with the initial shape that had been established to fit lily (*Lilium orientalis*) pollen. Comparison was done on the two-dimensional profile of the structure. This difference was quantified by calculating the difference between the initial and the final curves describing the cellular profile using the following algorithm. First, elongation of the cell was

calculated from the translation α of the apical pole in the y-direction:

$$\alpha = Y_{tip,step100} - Y_{tip,step0}.$$

Y coordinates of the points on the meridian determining the pollen tube profile after the 100th loading cycle were then corrected for tube elongation (in other words, the final and initial shapes were superimposed):

$$Y_{adjusted} = Y_{step100} - \alpha.$$

Then, the differences for each point on the curve were calculated by:

$$\Delta X = X_{step100} - X_{step0}$$

$$\Delta Y = Y_{adjusted} - Y_{step0}.$$

In the parameters described above, "tip" indicates the pole of the cell, "step 0" the original structure, and "step 100" the structure after 100 loading cycles. Finally, the deviation of a simulation from the initial shape was calculated by determining the average value for

$$\text{Shape change} = \sqrt{(\Delta X^2 + \Delta Y^2)}$$

for each coordinate of a given profile.

Pattern of Surface Deformation

In tip-growing cells, cell wall deformation caused by the effect of the internal hydrostatic pressure leads to a displacement of material points on the apical cell wall toward the outside, until the deformed wall becomes part of the nongrowing cylindrical shank (Dumais et al., 2004). The trajectory that a marker on the cellular surface describes during the deformation process reveals the strain pattern on the cellular surface (Dumais et al., 2004; E.R. Rojas and J. Dumais, unpublished data). An FE model that describes tip growth in a realistic manner will have to produce similar surface strain patterns. To test the simulations for their capacity to reproduce experimentally observed trajectories of surface markers, we fixed key points on the FE structure and followed their displacement over a sequence of load cycles.

This method is not trivial in a FE approach since during remeshing all nodes are redefined. Therefore, a single node cannot be followed over multiple load application and remeshing steps. Therefore, the position of a surface marker was extrapolated using the following approach. A point on the original structure was defined as surface marker, and its new position after a single load application was recorded. Following remeshing, the meridional coordinates of the surface marker in the new mesh were defined by identifying the two nearest nodes. The position of these two nodes was recorded, and the subsequent position of this point was maintained between the identified nodes for the next loading cycle. The position of the surface marker was approximated by assuming it to be in the center between the two neighboring nodes. This process was repeated with each loading cycle. The positions of the surface markers were then plotted to map their respective displacement trajectories.

For each simulation, displacement trajectories for five surface markers located at various distances from the pole of the cell were performed. The displacement trajectories were then compared with experimental results (E.R. Rojas and J. Dumais, unpublished data) in the same manner as the determination of the degree of self-similarity.

RESULTS

Identification of Crucial Parameters

Theoretical considerations suggest (Geitmann and Steer, 2006) and micromechanical data confirm (Geitmann et al., 2004; Zerzour et al., 2009) that the cell wall of a tip-growing cell has a higher degree of deformability at the apex than in the shank. However, neither the type of mechanical testing nor the spatial resolution of the microindentation approach lends itself to conclude on the precise spatial distribution of extensibility in the apex. Experimental studies (Parre and Geitmann, 2005a, 2005b; Aouar et al., 2010) corroborate that considerable mechanical support in the cylindrical shank of the cell prevents this region from swelling, but quantitative information is elusive. An objective of our study was to identify the theoretical distribution of material properties within the cell wall of the tip-growing cell that is necessary to produce a perfectly self-similar growth pattern. We posed two questions in particular: (1) How steep does the gradient in cell wall extensibility in the meridional direction have to be to obtain the initial shape defined by $r_L = 1.5\, r_T$? (2) Does the cell wall need to possess mechanical anisotropy in its plane? The second question arises from the observation that cellulose microfibrils are present in the apical region of pollen tubes (Sassen, 1964); thus, a biochemical basis for putative anisotropy exists.

To simulate extended periods of growth, an internal pressure load was applied repetitively to the FE structure. The resulting deformation depended on the distribution of material properties in the cell wall, or shell, which were determined by the set of rules detailed above. To identify crucial parameters leading to self-similar growth for the chosen initial shape, we generated an initial set of 64 parameter combinations by modulating three variables: the angles θ_i defining the spatial distribution of annular domains and multiplication factors m_T and m_L. The angles were varied such that their sum describing domains 1 through 6 equaled 90° (Figure 2D). For m_L, we tested the values 1.5, 2, 2.5, and 3, and m_T was tested for the values 0.5, 1, 2, 3, and 4. For all possible combinations of the explored variables, simulations consisting of 50 iterations were performed. To classify the results of this first set of simulations, we assessed the resulting structures for self-similarity by qualitatively comparing their shapes to that of the initial structure. Analyzing all 64 simulations revealed the following tendencies.

Modulation of m_L

Multiplication factor m_L directly influences the steepness of the gradient in cell wall extensibility from the pole toward the shank. When keeping m_T constant, high m_L caused the radius of the elongating tube to progressively decrease after repeated load cycles, and simultaneously, tube elongation per load cycle was reduced (Figure 3). By contrast, at low values for m_L, this tapering was less pronounced or, depending on m_T, resulted in a widening
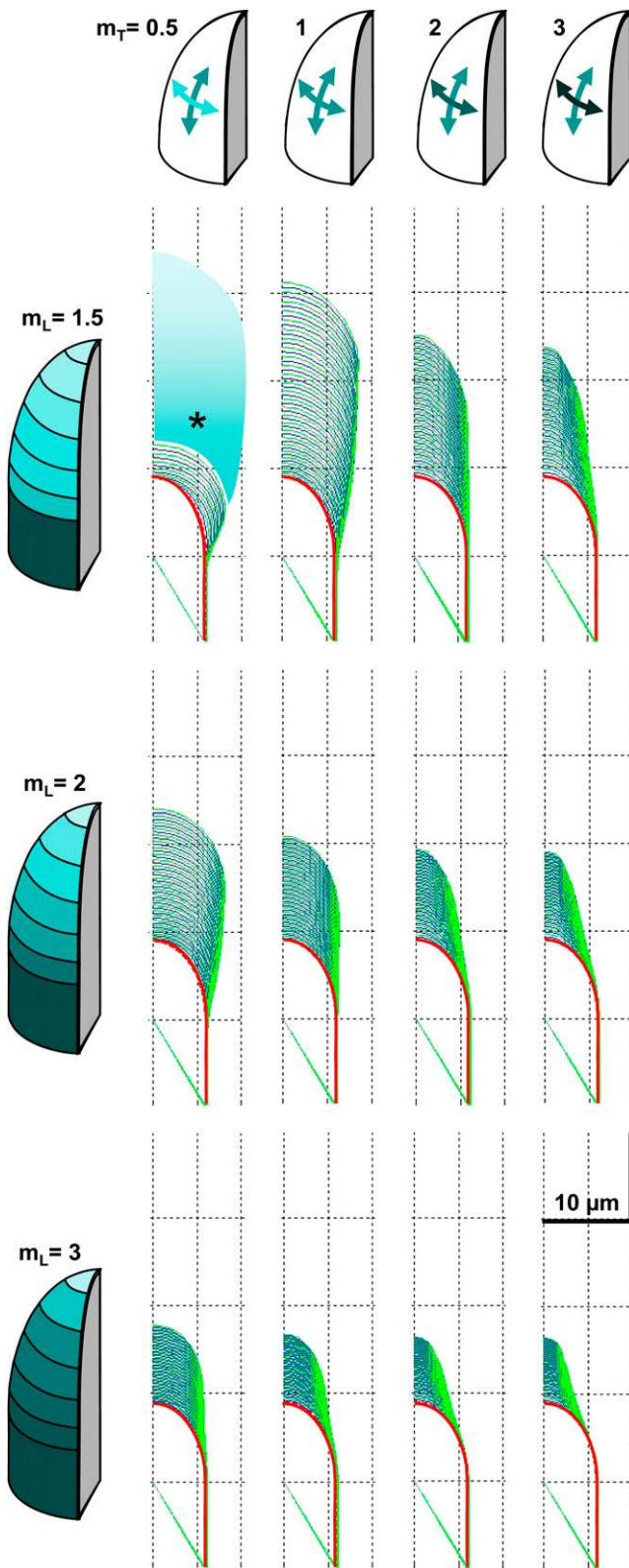
of the tube and an increased tube elongation. The optimal value of m_L that prevented the tube diameter from changing depended on m_T and the size distribution of the surface domains but was generally 2 or 2.5.

Modulation of m_T

Multiplication factor m_T determines the degree of anisotropy in cell wall extensibility. Increasing the Young's modulus in the circumferential direction ($m_T > 1$) resulted in a progressive reduction of the tube radius, whereas if the Young's modulus was lower in the circumferential than in the meridional direction ($m_T < 1$), tubes widened (Figure 3). Depending on m_L, different values for m_T resulted in a constant tube diameter after repeated load cycles. However, for $m_T > 1$, the apex became more prolate (pointed) (i.e., the ratio between r_L and r_T became higher), whereas for $m_T < 1$ the apex became oblate (flatter) (Figure 3). Only for $m_T = 1$ did we find combinations of the other parameters that resulted in true self-similarity for the given initial shape. Contrary to m_L, tube elongation per load cycle only changed moderately upon manipulation of m_T.

Size of Surface Domains

The shape of the gradient in cell wall extensibility in the meridional direction can be influenced by changing the size of individual surface domains through manipulation of the distribution of domain angles. The variation of domain angles affected both the degree of self-similarity and elongation rate of the pollen tube depending on m_L and m_T. Generally, large domain angles for either domain 1 or domain 2 caused swelling of the tube. In other words, if an increase in Young's modulus set is too far away from the pole of the tube, a widening of the elongating tube resulted.

Analysis of all 64 simulations allowed us to conclude that no self-similarity could be achieved when the cell wall material was anisotropic ($m_T < 1$ or $m_T > 1$) (Figure 3). Therefore, a second set of 32 simulations was performed in which m_T was kept constant (equal to 1 to maintain an isotropic distribution), while m_L and angle distribution were varied in the same ranges as previously, but using smaller increments (see Supplemental Table 1 online). Qualitative comparison revealed that overall shallow gradients (Figure 4A) or a large region of low Young's modulus around the pole (Figures 3 and 4B) caused the expanding tube to swell, whereas steeper gradients (Figure 4C) resulted in a reduction of the tube diameter of the elongating tube. Self-similarity was achieved by a number of different gradients or parameter combinations, all of which were characterized by a moderate but

Figure 3. Subset of Simulations Showing the Deformation of the Cell Wall Structure after 50 Load Cycles.

Different values for m_L (rows) and m_T (columns) were tested. Relative anisotropy defined by m_T values are also symbolized in the color shades of the arrows, with dark color standing for stiffer material properties. The profile of the original structure is indicated by the red line. Alternating blue and green lines indicate the results of repeated load cycles. In this subset, the domain angles were identical, with $\theta_i = 15°$ for $i = 1$ to 6. Various combinations of multiplication factors m_L and m_T demonstrate that for this particular angle distribution, self-similarity was obtained for $m_L = 2$ and $m_T = 1$. The asterisk indicates an error occurring after the 12th loading cycle due to instability in the structure.
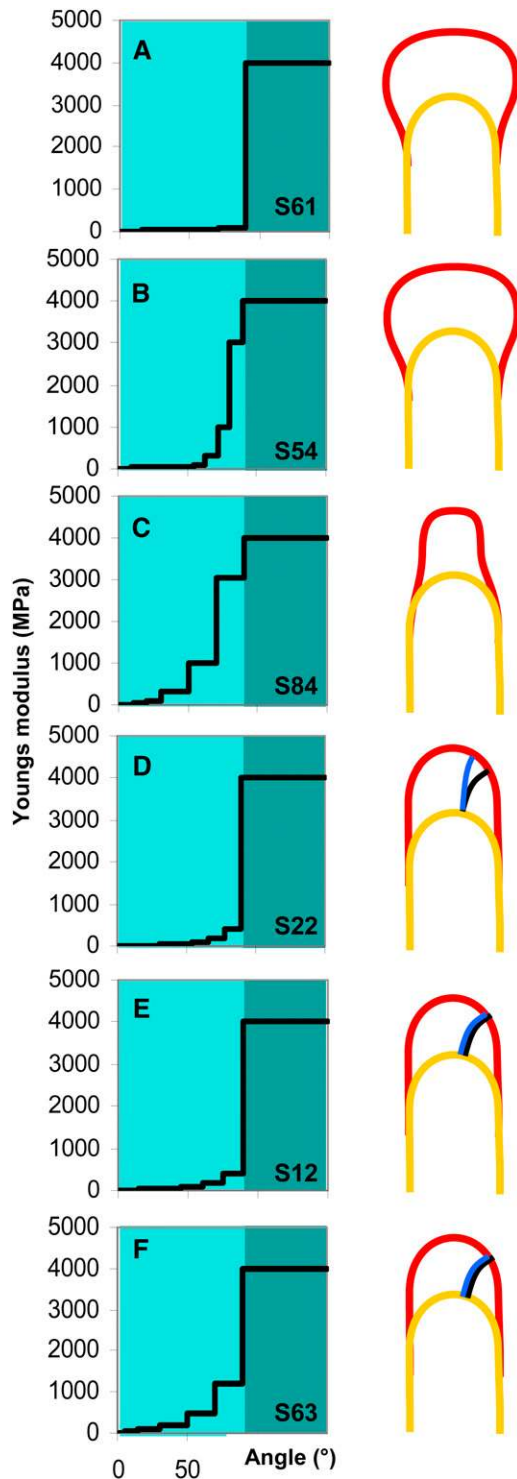
Figure 4. Spatial Distribution of the Young's Modulus in the Meridional Direction of a Representative Subset of Simulations.

For all simulations, $m_T = 1$. The apical dome (domains 1 to 6) is indicated with light teal and the cylindrical shank with dark teal (domain 7). Swelling of the apex could be caused by a shallow gradient **(A)** or by a large polar domain with low Young's modulus and a late onset in the increase of the

steady increase in Young's modulus from domain 1 to 6 and by a significant jump in Young's modulus from domain 6 to domain 7 (Figures 4D to 4F). Within this second set of simulations, the eight parameter combinations with the highest degree of self-similarity were selected based on qualitative comparison (see Supplemental Table 1 online) and subjected to further analyses.

Quantitative Validation of Selected Parameter Combinations

The eight simulations selected were analyzed quantitatively for their degree of self-similarity (Figures 5A and 5B) and for their surface strain patterns (Figures 5C and 5D) as explained in the Validation of the model. As expected, the eight simulations displayed only minor differences in self-similarity (red bars, Figure 5E), but they differed significantly in the quality of their surface strain patterns. The two simulations showing the highest degree of self-similarity with a good strain pattern fit were characterized by a steady increase in Young's modulus beginning close to the pole of the cell and a significant jump of the modulus between domains 6 and 7 (Simulation S12, Figure 4E; Simulation S63, Figure 4F). The spatial distribution of stress within the tube revealed that the overall stress in the wall of the cylindrical region of the cell is significantly higher than at the pole (Figure 5F). The boundaries between surface domains experience small local stress maxima due to the discrete change in mechanical properties (ring-shaped color changes in Figure 5F). However, these do not significantly affect the deformation of the structure, as the pattern of the overall strain is nevertheless gradual (Figure 5G). The strain pattern shows highest deformation in the pole region and no deformation in the distal region of the tube. The fact that the strain gradient is oriented in opposite direction to the stress gradient is a consequence of the strong difference in mechanical properties between the two regions.

Effect of Geometry and Turgor Pressure

Once we had established gradients in cell wall mechanical properties leading to self-similar growth, swelling, or tapering, we wanted to assess the effects of cellular geometry and pressure load on the behavior of the model. We generated a new set of simulations based on the mechanical gradients in simulations S12 (self-similar), S51 (swelling), and S14 (tapering) and varied cell size, cell wall thickness, and turgor pressure in ranges that were biologically relevant. Within the ranges tested, none of these parameters affected the qualitative nature of the shape change

modulus **(B)**. Tapering was caused by a steeper gradient **(C)**. Self-similar growth could be achieved by various parameter combinations (**[D]** to **[F]**), but these did not necessarily produce the surface strain patterns observed in growing pollen tubes **(D)**. The simulations producing a good fit with these strain patterns (**[E]** and **[F]**) showed a steady, moderate increase in the Young's modulus within the apical dome and a sudden jump at the transition region to the shank. Yellow line indicates original shape of the cell, and the red line shows tube shape after repeated load cycles. Blue lines indicate paths of surface markers obtained from the simulation, and black lines show experimental data obtained from E.R. Rojas and J. Dumais (unpublished data).
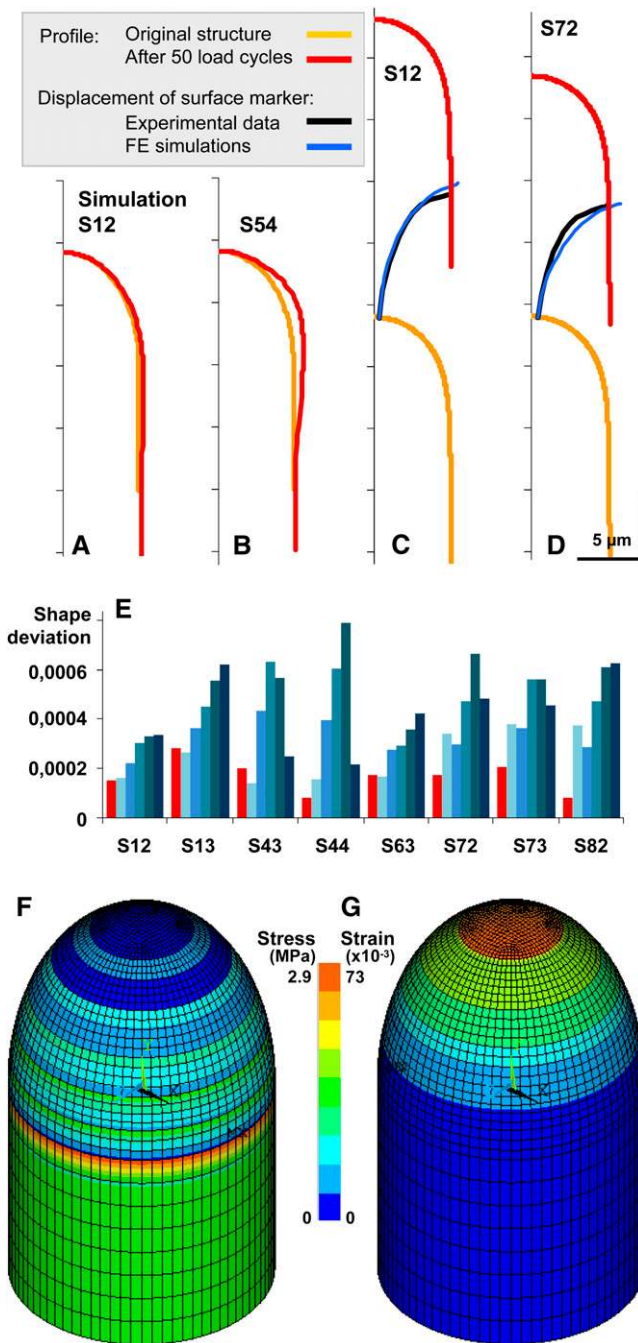
Figure 5. Quantitative Validation of Simulations.

(A) and **(B)** Self-similarity was assessed quantitatively by comparing the shape profile of a tube after 100 loading cycles (red) with the original structure (orange). Self-similarity was excellent for several simulations (e.g., S12; [A]), but in most others, the resulting shape was very different from the original shape (e.g., S54; [B]).
(C) and **(D)** Surface deformation was assessed by comparing the paths of surface markers obtained from the simulation (blue) with experimental data obtained from E.R. Rojas and J. Dumais (unpublished data) (black). Only a few simulations showed very good agreement between both curves (e.g., S12; [C]), whereas others showed varying degrees of

after 50 iterations of the load cycle. Using the mechanical gradient determined for simulation S12, self-similarity was always achieved independently of the thickness of the cell wall (as long the thickness was defined as being identical in all surface domains), the diameter of the tube, and the applied turgor pressure (Figure 6). The same was true for swelling and tapering behavior (Figure 6). The only factor affected was the increase in tube length per load cycle. Higher turgor pressure increased this length, and lower pressure reduced it in a linear manner.

Cell wall thickness was varied within a range that maintained the wall relatively thin compared with the tube diameter, as is typical for plant cells with primary cell walls. An increase in cell wall thickness reduced tube elongation per load cycle in a linear manner (Figure 6).

Cell size was altered while maintaining the ratio between the long (r_L) and the short radii (r_T) of the apical prolate spheroid. An increase in tube diameter resulted in a significant increase in tube length per load cycle. Unlike turgor pressure and cell wall thickness, which resulted in a linear response, the increase in tube growth was approximately proportional to r_T^2 (Figure 6). The reason for this phenomenon is likely to be that the deformation depends on the total force exerted on the apical cell wall by the pressure, which is linearly dependent on the cross section of the tube, which in turn scales with r_T^2. It is important to note that in a quasistatic model such as this version, the observed changes in tube elongation per load application do not allow any conclusion regarding growth rate.

Finally, we used the three parameter combinations that generate different shapes to confirm that the FE structure representing the quarter of the tube (90° structure) behaved identically to the full tube (360° structure). Comparison of the resulting shapes and displacements demonstrated that both structural approaches yielded exactly the same results (Figure 6).

Comparison with Experimentally Determined Spatial Distribution of Cell Wall Components

We wanted to assess whether the steady mechanical gradient in the apical dome of the pollen tube and the steep increase in Young's modulus in the transition region between the dome and the shank were reflected in the biochemical composition of the

deviation from the experimental data (e.g., S72; [D]).
(E) Quantitative assessment of the quality of eight simulations previously selected based on qualitative inspection. The red bars indicate the deviation from self-similarity. The blue bars indicate the deviations in the displacement trajectories of five surface markers per simulation.
(F) Distribution of local stresses upon load application on the surface of the 360° structure using parameter combination S12. Blue indicates low stress at the pole and green higher stress in the shank. Ring-shaped regions of locally increased stress (green, yellow, and orange) are due to discrete steps in Young's modulus between surface domains, inherent to the approximate approach chosen here.
(G) Distribution of local strain upon load application on the surface of the 360° structure using parameter combination S12. Blue color indicates low or absent strain in the shank, and orange indicates high strain at the pole. Despite the stress artifacts observed in **(F)**, the strain distribution is rather gradual and does not show local maxima.
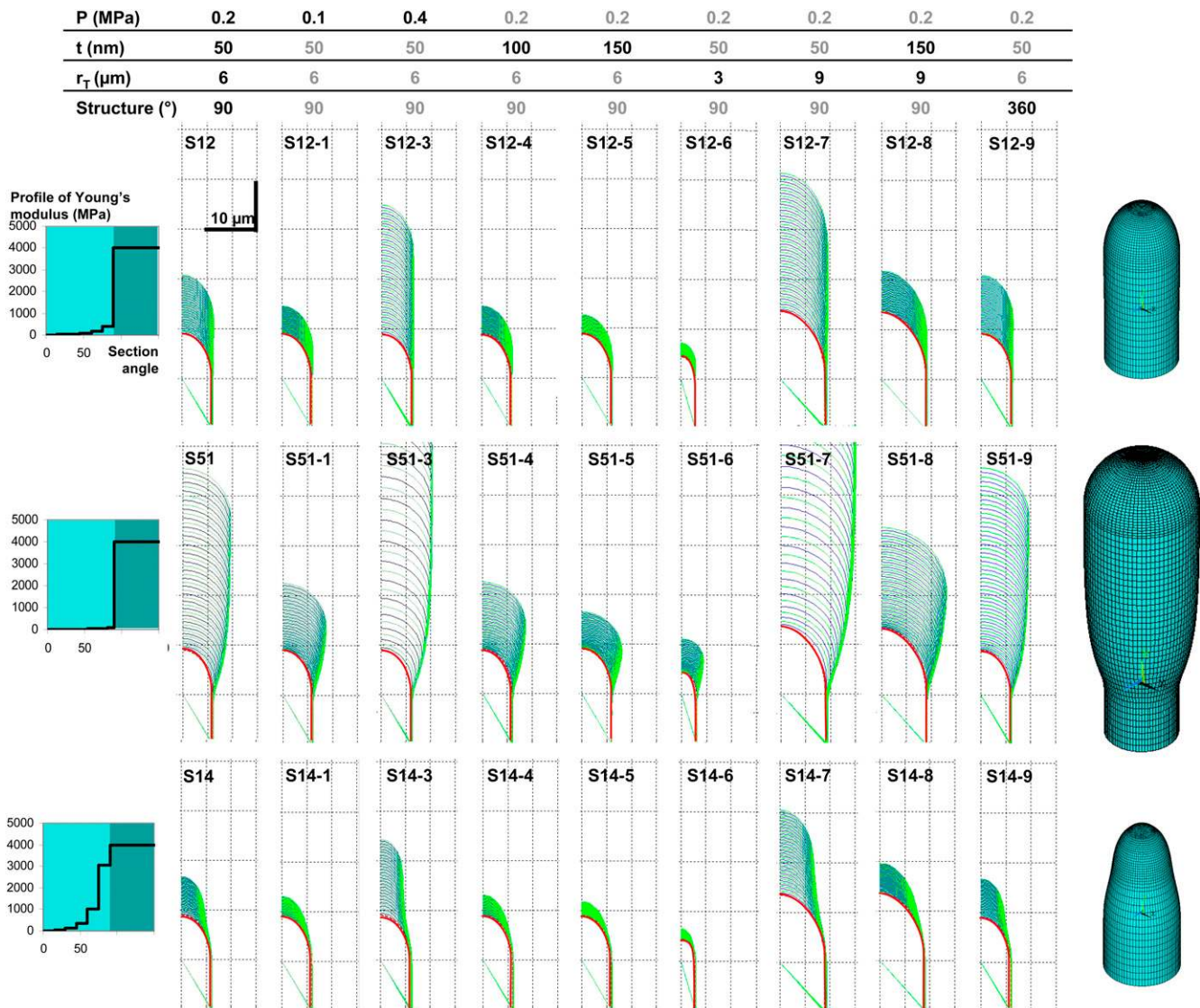
Figure 6. Effect of Cell Wall Thickness, Turgor Pressure, Tube Radius, and Structure on the Growth Pattern.

Cell wall thickness t, turgor pressure P, and tube radius r_T were altered in biologically relevant ranges to test their effect on deformation geometry. The nature of apical deformation (self-similar, swelling, and tapering) was not affected by any of the three parameters. The only characteristic altered was the increase in tube length per loading cycle. Simulations performed with a 360° structure demonstrated that it behaved identically to the corresponding 90° structure. All graphs show length profiles. The graphs on the left show the gradient in mechanical properties used for the respective simulations, as determined by m_L and the size distribution of the surface domains. Light teal indicates the apical dome and dark teal the cylindrical shank. The right column shows three-dimensional representations of the 360° structures. The profile of the original structure is indicated by the red line. Alternating blue and green lines indicate the results of repeated load cycles. In all simulations, $m_T = 1$.

cell wall. Pollen tubes are known to display a nonuniform distribution of cell wall components along the longitudinal axis of the cell (Li et al., 1994; Geitmann and Parre, 2004; Parre and Geitmann, 2005a, 2005b), but quantitative data are lacking. To quantify the precise spatial distribution of cell wall components in lily pollen tubes, a common model species, we labeled cellulose, callose, and pectins in in vitro–grown tubes and quantified the relative fluorescence intensity along the perimeter of the cell (Figure 7). In accordance with other pollen tube species (Li et al.,

1994, 1995; Parre and Geitmann, 2005a), our fluorescence micrographs show that the entire lily tube was surrounded by a layer of pectic polysaccharides. In the apical region, these pectins were highly methylesterified, whereas they were increasingly deesterified in the more mature region of the cell wall. The abundance of cellulose did not change significantly over the length of the tube, whereas that of callose increased slowly, starting in the subapical region. Quantification of the fluorescence micrographs revealed that the most dramatic changes in
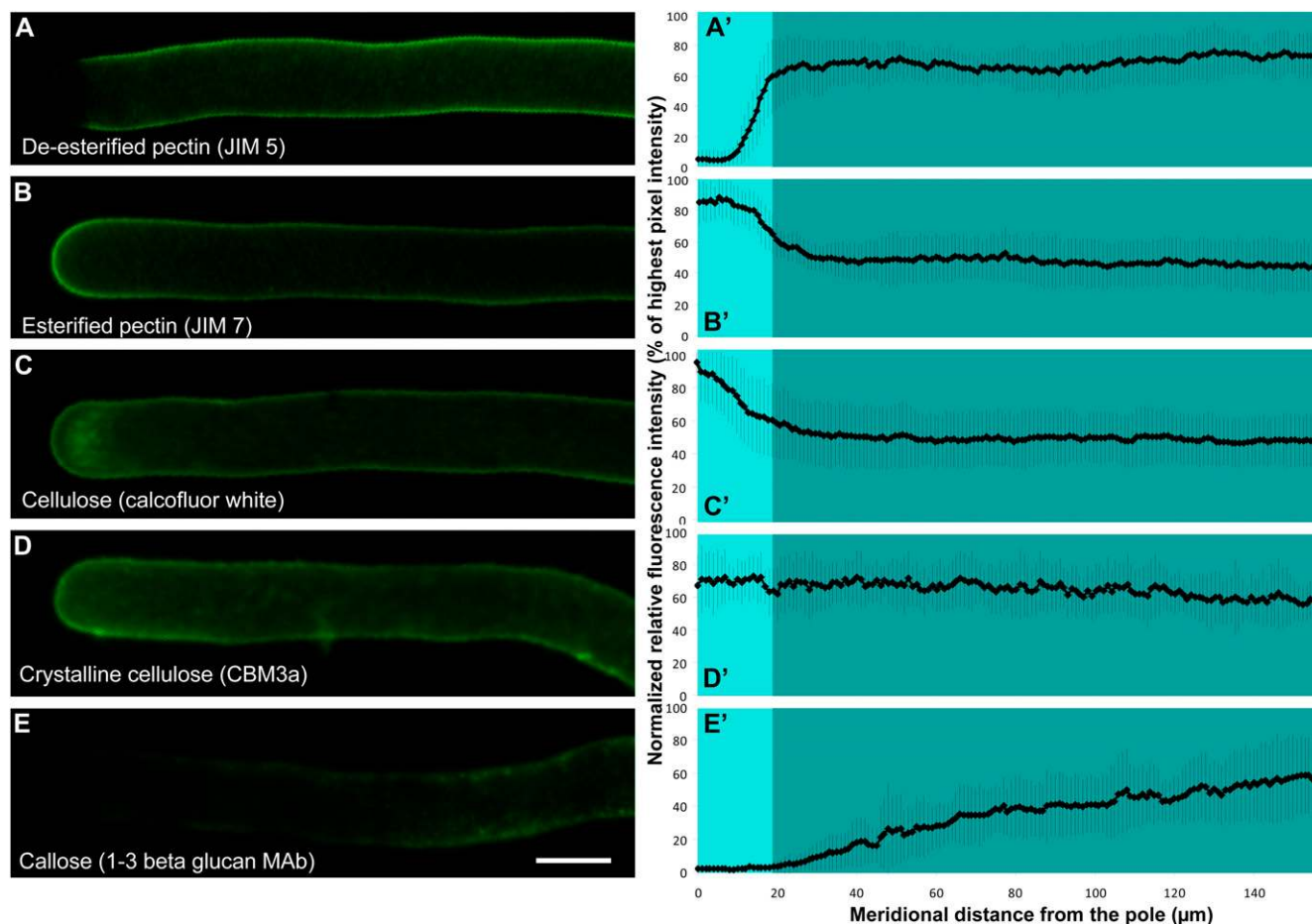
Figure 7. Spatial Distribution of Cell Wall Components in in Vitro–Growing Lily Pollen Tubes.

Cells were treated with specific antibodies and histochemical stains for pectins with a low **(A)** and high **(B)** degree of esterification, cellulose **(C)**, crystalline cellulose **(D)**, and callose **(E)**. Graphs **(A')** to **(E')** show the corresponding relative fluorescence intensity along the perimeter of the cell, normalized for each tube, and averaged over at least 10 tubes. Vertical bars are standard errors. Light teal indicates the apical dome and dark teal the cylindrical shank. Bar = 20 μm.

cell wall biochemistry occurred between 15- and 20-μm meridional distance from the pole of the cell (Figure 7). Given the typical diameter of 18 to 21 μm for lily pollen tubes, this position corresponded exactly to the transition zone between the apical dome and cylindrical shank of the cell (marked by a change in background color in the graphs). Importantly, the configuration of pectins changed from a high to a low degree of methylesterification at this location, which allows their gelling through calcium ions, a process that rigidifies the extracellular matrix. In particular, the distribution of deesterified pectins (Figure 7A) showed remarkable similarity to the curve described by the distribution of mechanical properties established by the FE model (Figures 4E and 4F).

Removal of Pectin Disturbs Cell Shape Determination

Given the excellent correlation between predictions made by the FE model and spatial distribution of pectin label, we wanted to test the role of this cell wall component in determining cell shape. To

this end, we exposed pregerminated lily pollen tubes to pectinase for 15 min. As a result, pollen tubes developed dramatic swellings in the apical region (Figure 8). The virtual absence of fluorescence after immunolabel with JIM5 (Figure 8A) and JIM7 (micrographs completely black; data not shown) demonstrated the successful digestion and hence removal of a significant portion of the pectin moiety from the pollen tube cell wall.

An FE simulation performed using identical mechanical properties (Young's modulus 50 MPa) for all surface domains of the tube confirmed that an absence of a mechanical gradient in the cell wall is predicted to lead to a spherical swelling (Figure 8E).

DISCUSSION

Mechanics of Growth in Walled Cells

Growth in walled cells is driven by the internal turgor pressure. However, since turgor is a nonvectorial force, spatial regulation
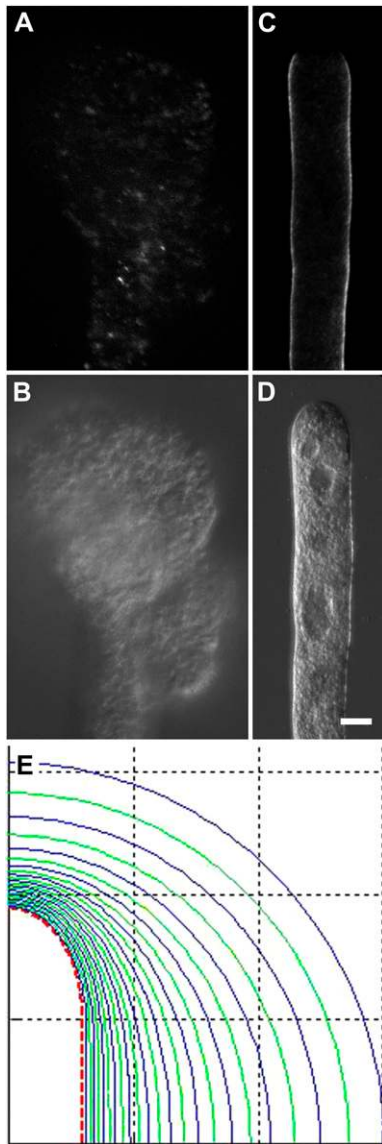
Figure 8. Effect of Pectin Digestion on Pollen Tube Shape.

(A) to **(D)** Pregerminated pollen tubes were treated with pectinase for 15 min (**[A]** and **[B]**). Pollen tubes exposed to the enzyme were swollen at the apex **(A)**, whereas untreated tubes elongated in self-similar manner **(C)**. Immunofluorescence label with JIM5 revealed the near absence of pectins with a low degree of methylesterification in enzyme-treated samples **(B)** compared with the control tubes not treated with the enzyme **(D)**. Note that the images should not be compared quantitatively since in order to reveal residual label in the enzyme-treated samples, exposure time had to be at least tripled compared with the control sample. Fluorescence micrographs (**[A]** and **[C]**) and corresponding differential interference contrast micrographs (**[B]** and **[D]**). Bar = 10 μm. **(E)** FE simulation using identical Young's modulus for surface domains 1 through 7 resulted in spherical swelling of the structure. The profile of the original structure is indicated by the red, dashed line. Alternating blue and green lines indicate the results of repeated load cycles.
[See online article for color version of this figure.]

of the growth process relies on the mechanical properties of the cell wall (Cosgrove, 2005; Geitmann and Ortega, 2009). As predicted (Geitmann and Steer, 2006), micromechanical data revealed a difference in mechanical behavior between the tip of a growing pollen tube and its cylindrical shank (Geitmann and Parre, 2004 Bolduc et al., 2006; Zerzour et al., 2009). It had been known from other plant species that this gradient is generated by the absence or scarcity of callose (Parre and Geitmann, 2005b) and cellulose (Aouar et al., 2010) at the growing apex as well as by the relatively high degree of esterification of the pectin polymers in this region (Parre and Geitmann, 2005a, 2005b). The pectic polymers are secreted at the apex of the cell in a highly methylesterified form, which renders them essentially liquid; consequently, the cell wall is easily deformable in this region. During maturation of the wall, pectin methylesterase, an enzyme that is secreted together with the cell wall polymers, cleaves off the methyl groups. The resulting negative charge of the pectin molecules attracts calcium ions, which cause the polymers to gel and thus to form a matrix of much higher stiffness. Although numerous immunofluorescence studies on pollen tubes have confirmed the general biochemical differences between the nongrowing shank and growing apex (Li et al., 1994, 1995; Derksen et al., 2002; Bosch et al., 2005; Parre and Geitmann, 2005a, 2005b; Aouar et al., 2010), the spatial distribution of biochemical components within the apical dome has not previously been published. The quantitative data presented here reveal that the most significant changes in the biochemical composition occur in the transition region between the apical dome and tubular shank of the cell. These changes were particularly dramatic in the distribution of pectins with a low degree of esterification. The striking similarity of their distribution with the profile of the Young's modulus established using the FE simulations confirms the importance of the change in pectin conformation for the geometry of the elongating tube. The reduction of the pectin moiety in the pollen tube cell wall through the external application of pectinase and the resulting swelling corroborated further that the presence of the mechanical gradient generated by the changing pectin chemistry is crucial for shape determination in this cell.

Information Gained from the FE Approach

Our model has allowed us to draw a number of conclusions that reveal important details about the mechanical principles governing tip growth. The highest degree of self-similarity was achieved when representing the cell wall as having isotropic mechanical properties. This finding does not seem to be consistent with observations in root hairs in which a slight meridional stiffening (corresponding to $m_T < 1$) provides the best explanation for tip elongation (Dumais et al., 2004). However, unlike the lily pollen tube analyzed here, the shape of a root hair is somewhat oblate with a region of maximal curvature at an annular region around the pole of the cell. Consequently the mechanics of the growth process in this cell type may be slightly different. Furthermore, the increments in m_T tested here were too large to pick up a subtle anisotropy that could putatively provide an even better fit than those simulations we identified in this set. It remains that the result of our approximate approach is consistent with structural

observations. Putative anisotropy would have to derive from a preferential orientation of microfibrils. Cellulose orientation has unfortunately not been determined in the apical dome of lily pollen tubes, although our immunolabel shows that cellulose is present in this region. However, in other plant species, microfibrils seem to be short and oriented randomly in the apical region of the pollen tube (O'Kelley and Carr, 1954; Sassen, 1964; Derksen et al., 1999), indicating that they do not generate anisotropy in the cell wall mechanical properties of the tube apex.

More than one parameter combination tested here produced growth patterns with an acceptable degree of self-similarity, but not all of them necessarily generated trajectory maps of surface markers that agreed with experimental data. Agreement was obtained for steady mechanical gradients in the apical dome that were followed by sudden increases in Young's modulus in the transition region to the shank. Therefore, it is important to recognize that testing for similarity between the predicted and experimentally observed final shape of a growing structure is not sufficient to identify the correct mechanical profile. Our second validation method, the comparison with surface strain patterns, was therefore crucial to determine the fit of the model with the living cell.

Our model showed that swelling of the tube was achieved when the gradient in Young's modulus along the longitudinal axis was not sufficiently steep or when the increase in Young's modulus began too far from the pole. This is consistent with experimental data showing that enzymatic treatments with cellulase, an enzyme that digests cellulose microfibrils, result in a swelling of the tube apex (Aouar et al., 2010). The FE simulations suggest that the effect is mediated by a reduction in the Young's modulus in the apical dome. This means that, although they may not confer anisotropy to the pollen tube apex due to their random orientation, the presence of cellulose microfibrils nevertheless seems to contribute to tensile resistance of the cell wall in this region. Similarly, the FE model may help to explain other phenomena that occur upon manipulation of the mechanical properties of the pollen tube cell wall, such as those caused by the transient expression of pectin methylesterase inhibitor, by the overexpression of pectin methylesterase (Röckel et al., 2008), or by exposure to externally applied enzyme (Bosch et al., 2005; Parre and Geitmann, 2005a). Ongoing controversies about the cellular features that regulate growth dynamics in these cells (Zonia et al., 2006; Zonia and Munnik, 2009; Winship et al., 2010) may also gain from this engineering approach to cell biology.

Impact of a Mechanical Model of Tip Growth

An accessible mathematical model will draw attention to the fact that any kind of change in growth behavior is ultimately mediated by affecting cell mechanics. Recognizing this should complement approaches that hitherto focused purely on intracellular processes, such as signaling events. Pollen tube swelling (Kost et al., 1999; Klahre et al., 2006; Klahre and Kost, 2006; Hwang et al., 2010) or tapering (Klahre and Kost, 2006) resulting from manipulations in the signaling machinery of the cell can only be completely understood if the biophysical mechanism that translates biochemical and signaling processes into particular cellular

phenotypes are included in the interpretation of experimental data.

A significant advantage of the FE approach is the fact that the model can easily be adapted to other tip-growing cell types. Species-specific differences in the spatial distribution of biochemical components can easily be accommodated, rendering the model extremely versatile. Variations in geometry, such as tube diameter and shape of the apex, can be modified through modulating a single parameter, respectively. Hence, adaptation to the small tubes of *Arabidopsis thaliana* (typical diameter of 6 μm) or to the more tapered tip of fungal hyphae is straightforward. The gradient of mechanical properties and the degree of anisotropy can be altered locally or globally, and the model can be equipped with a time-dependent component using viscoelastic instead of purely elastic properties.

Limitations of the FE Approach

Pollen tube growth is a very rapid process, and the deformation of the cell wall involved in the process is extremely large compared with the size of the initial structure. One of the drawbacks of the FE approach in the context of large deformation was the necessity of operating with cyclic iterations, which implies that a deformation is achieved through a series of small, discrete steps. During each iterative step, the structure was recreated, and, depending on the number of nodes, the shape of the subsequent structure could display small differences compared with the previous structure (e.g., anchor points of the geometry could change). However, given the mesh density we used here, these errors were orders of magnitude smaller than the dimension of the structure.

Another potential shortcoming of our FE approach was the spatial distribution of material properties in discrete domains. As a result, there were significant and instant changes in the elastic modulus between the successive, ring-shaped cell wall domains. These introduced local stress maxima in the cell wall (Figure 5F). However, even after 100 iterations, the resulting structures always had smooth curvatures and the overall strain patterns were gradual (without local maxima). This suggests that these local stresses had negligible effects on the final outcome. Further confirmation of the validity of our model can be derived from comparison with other mathematical approaches. Our profiles for the Young's modulus look remarkably similar to those obtained for spatial distribution of mechanical properties in root hairs that had been generated inferring from a comparison of the strain rates and wall stresses in this cell type (Dumais et al., 2004). Therefore, despite the discrete changes in mechanical properties, our approximate approach was sufficient to yield an excellent qualitative fit with experimental data.

Potential of the FE Approach for Modeling Complex Geometries

Previous attempts to model tip growth were mostly restricted to geometric interpretations (Da Riva Ricci and Kendrick, 1972) or purely mathematical equations (Denet, 1996). However, although they may be elegant in their simplicity, their biological relevance is limited due to the low number of parameters. For

instance, cell wall thickness or anisotropy is not taken into account in these models. More recent models include the vesicle supply center model for hyphal growth (Bartnicki-Garcia et al., 2000), hyphal growth models based on linear elastic (Goriely and Tabor, 2003a) and nonlinear elastic membrane theory (Goriely and Tabor, 2008), a model for root hair elongation based on viscoplasticity theory (Dumais et al., 2006), and an approach based on a representation of the cell wall as a viscous fluid shell (Campàs and Mahadevan, 2009). However, all of these models are limited in their versatility to the simple axisymmetric geometry of the tip-growing cell, even though they can explain variations in shape that are based on changes in the tube diameter or the pointedness of the apex.

The most important advantage of the FE approach is its potential to cope with the complexity of cellular geometries and mechanical properties encountered in nature. In most of the mentioned models, the thickness of the cell wall is only indirectly considered, whereas in the FE model, this variable can be manipulated either globally or, with minor modifications, locally, to accommodate phenomena such as the temporal variation in the thickness of the apical cell wall observed in lily and tobacco (*Nicotiana tabacum*) pollen tubes (McKenna et al., 2009; Zerzour et al., 2009). Remarkably, this experimentally observed change in cell wall thickness is associated with temporary growth arrest or periodic temporal changes in the growth rate. Therefore, our model has the potential to explain these phenomena at the mechanical level and thus provides a tool to test conceptual models that explain processes, such as those displayed during oscillatory growth (Chebli and Geitmann, 2007; Zonia and Munnik, 2009). Potential integration with mechanical models operating at the molecular scale offers another intriguing perspective (MacKintosh et al., 1995; Wilhelm and Frey, 2003). This would allow us to predict cellular behavior based on the mechanical interaction and behavior of the polymers forming the cell wall (Kha et al., 2010).

More importantly, contrary to other models, the FE approach will enable us to model changes in the growth pattern that abandon axisymmetric geometry, such as a change in growth direction. This is a phenomenon that is typical of fungal hyphae and pollen tubes, as these cells are able to follow chemical gradients (Geitmann and Palanivelu, 2007). Asymmetric and other complex geometric shapes can be constructed in FE analysis based on three-dimensional data obtained from confocal imaging or other three-dimensional reconstruction techniques. Contrary to earlier models for tip growth, adaptation of the FE model is therefore not limited to tip growth. All the complex cellular shapes that can be observed in plant tissues are likely based on the nonuniform distribution of cell wall components and cell wall dimensions, and, as a consequence, the mechanical behavior. Shapes such as those of jigsaw puzzle–shaped epidermis cells could be modeled easily exploiting the discrete approach we used here that is based on the division of the cellular surface into domains with varying mechanical properties. The ability of the FE method to take a complex problem or structure whose solution may be difficult if not impossible to obtain and decompose it into smaller elements allows us to construct simple approximations of the solution that might provide important information on the mechanics of expansive cellular growth in all cell types with walls.

METHODS

Plant Material and Pollen Culture

Lily (*Lilium orientalis*) pollen was obtained from a local flower shop. Pollen was dehydrated for 24 h and then stored at $-80°C$ until use. Pollen grains were hydrated for 30 min. Hydrated pollen was incubated at $25°C$ for 2 to 3 h under continuous slow shaking on a shaker in a 25-mL Erlenmeyer flask containing 3 mL of growth medium made of 100 mg·mL^{-1} H_3BO_3, 300 mg·mL^{-1} $Ca(NO_3)_2 \cdot H_2O$, 100 mg·mL^{-1} KNO_3, 200 mg mL^{-1} $MgSO_4 \cdot 7H_2O$, and 50 mg·mL^{-1} sucrose.

Pollen tubes exposed to pectinase were grown in regular growth medium for 3 h and 45 min before the addition of 8 mg/mL pectinase (Fluka).

Fluorescence Label

All incubation and washing steps of the following protocol were performed in the microwave oven (Pelco BioWave 34700 equipped with a Pelco Cold Spot) operating at 150 W under 21 inches of Hg vacuum at a controlled temperature of $30 \pm 1°C$. For fluorescence labeling, pollen tubes were filtered and subsequently fixed in 3.5% freshly prepared formaldehyde in PIPES buffer (50 mM PIPES, 1 mM EGTA, and 0.5 mM $MgCl_2$, pH 6.9) for 40 s followed by three washes in PIPES buffer. For immunolabeling, pollen tubes were then washed three times with PBS buffer (135 mM NaCl, 6.5 mM Na_2HPO_4, 2.7 mM KCl, and 1.5 mM KH_2PO_4, pH 7.3) with 3.5% BSA. All subsequent washes were done with PBS buffer with 3.5% BSA for 40 s. All antibodies were diluted in PBS buffer with 3.5% BSA. Ten-minute incubations with the primary antibody were followed by wash steps and 10-min incubations with 1% IgG-Alexa Fluor 594 anti-rat secondary antibody (Molecular Probes). Controls were performed by omitting incubation with the primary or secondary antibody. Pectin labeling was performed with primary antibodies JIM5 (detects pectin with a low degree of esterification) and JIM7 (detects pectin with a high degree of esterification). Labeling for crystalline cellulose was done with CBM3a (Cellulose Binding Module 3a) followed by monoclonal mouse-antipolyhistidine antibody (Sigma-Aldrich). These primary antibodies were obtained from Paul Knox (University of Leeds, UK). Callose labeling was performed with monoclonal IgG antibody to $(1 \rightarrow 3)$-β-glucan (Biosupplies Australia). Cellulose (crystalline and amorphous) was also labeled with 1 mg mL^{-1} calcofluor following fixation. All samples were mounted on glass slides in a drop of citifluor (Electron Microscopy Sciences) for microscopy observation.

Fluorescence Microscopy

Observation of samples was done with a Zeiss Imager-Z1 microscope equipped with structured illumination microscopy (ApoTome Axio Imager), a Zeiss AxioCam MRm Rev.2 camera, and AxioVision Release 4.5 software. Observations were made using a filter set with excitation band-pass 450 to 490 nm, beamsplitter FT 510 nm, and emission band-pass 515 to 565 nm for calcofluor labeling and a filter set with excitation band-pass 390/22 nm, beamsplitter FT 420 nm, and emission band-pass 460/50 nm for Alexa fluor 594 detection. Exposure time was adjusted for all images so that only one or two pixels were saturated when not using the ApoTome imager. The ApoTome imager was then inserted into the light path and z-stack images of 1-μm intervals of pollen tubes were taken, and image reconstruction was performed using the AxioVision software by the projection of the stacks.

Image Processing and Fluorescence Quantification

Only z-projections were used for fluorescence quantification. ImageJ software (National Institutes of Health) was used for fluorescence quantification of the stained cell wall components. Pixel intensity was

measured along the periphery of each pollen tube, beginning from the pole. Values for fluorescence intensity were normalized to the highest fluorescence value for individual tubes before averaging ($n > 10$ for each sample). Distances on the x axis of the graphs represent the meridional distance from the pole of the cell.

Supplemental Data

The following materials are available in the online version of the article.

Supplemental Table 1. Parameter Settings Used for the Second Set of Simulations.

ACKNOWLEDGMENTS

REFERENCES

Aouar, L., Chebli, Y., and Geitmann, A. (2010). Morphogenesis of complex plant cell shapes - The mechanical role of crystalline cellulose in growing pollen tubes. Sex. Plant Reprod. **23:** 15–27.

Bartnicki-Garcia, S. (2002). Hyphal tip growth: Outstanding questions. In Molecular Biology of Fungal Development, H.D. Osiewacz, ed (New York: Marcel Dekker), pp. 29–58.

Bartnicki-Garcia, S., Bracker, C.E., Gierz, G., Lopez-Franco, R., and Lu, H. (2000). Mapping the growth of fungal hyphae: Orthogonal cell wall expansion during tip growth and the role of turgor. Biophys. J. **79:** 2382–2390.

Baskin, T. (2005). Anisotropic expansion of the plant cell wall. Annu. Rev. Cell Dev. Biol. **21:** 203–222.

Benkert, R., Obermeyer, G., and Bentrup, F.W. (1997). The turgor pressure of growing lily pollen tubes. Protoplasma **198:** 1–8.

Bolduc, J.F., Lewis, L., Aubin, C.E., and Geitmann, A. (2006). Finite-element analysis of geometrical factors in micro-indentation of pollen tubes. Biomech. Model. Mechanobiol. **5:** 227–236.

Bosch, M., Cheung, A.Y., and Hepler, P.K. (2005). Pectin methylesterase, a regulator of pollen tube growth. Plant Physiol. **138:** 1334–1346.

Campàs, O., and Mahadevan, L. (2009). Shape and dynamics of tip-growing cells. Curr. Biol. **19:** 2102–2107.

Chanliaud, E., Burrows, K.M., Jeronimidis, G., and Gidley, M.J. (2002). Mechanical properties of primary plant cell wall analogues. Planta **215:** 989–996.

Chanliaud, E., and Gidley, M.J. (1999). *In vitro* synthesis and properties of pectin/*Acetobacter xylinus* cellulose composites. Plant J. **20:** 25–35.

Chebli, Y., and Geitmann, A. (2007). Mechanical principles governing pollen tube growth. Funct. Plant Sci. Biotechnol. **1:** 232–245.

Cosgrove, D.J. (2005). Growth of the plant cell wall. Nat. Rev. Mol. Cell Biol. **6:** 850–861.

Da Riva Ricci, D., and Kendrick, B. (1972). Computer modelling of hyphal tip growth in fungi. Can. J. Bot. **50:** 2455–2462.

Denet, B. (1996). Numerical simulation of cellular tip growth. Physiol. Rev. **53:** 986–992.

Derksen, J., Knuiman, B., Hoedemaekers, K., Guyon, A., Bonhomme, S., and Pierson, E.S. (2002). Growth and cellular organization of *Arabidopsis* pollen tubes *in vitro.* Sex. Plant Reprod. **15:** 133–139.

Derksen, J., Li, Y.-Q., Knuiman, B., and Geurts, H. (1999). The wall of *Pinus sylvestris* L. pollen tubes. Protoplasma **208:** 26–36.

Dumais, J., Long, S.R., and Shaw, S.L. (2004). The mechanics of surface expansion anisotropy in *Medicago truncatula* root hairs. Plant Physiol. **136:** 3266–3275.

Dumais, J., Shaw, S.L., Steele, C.R., Long, S.R., and Ray, P.M. (2006). An anisotropic-viscoplastic model of plant cell morphogenesis by tip growth. Int. J. Dev. Biol. **50:** 209–222.

Dyson, R.J., and Jensen, O.E. (2010). A fibre-reinforced fluid model for anisotropic plant cell growth. J. Fluid Mech. **655:** 472–503.

Geitmann, A., McConnaughey, W., Lang-Pauluzzi, I., Franklin-Tong, V.E., and Emons, A.M.C. (2004). Cytomechanical properties of *Papaver* pollen tubes are altered after self-incompatibility challenge. Biophys. J. **86:** 3314–3323.

Geitmann, A., and Ortega, J.K.E. (2009). Mechanics and modeling of plant cell growth. Trends Plant Sci. **14:** 467–478.

Geitmann, A., and Palanivelu, R. (2007). Fertilization requires communication: Signal generation and perception during pollen tube guidance. FOB Biotechnol. **1:** 77–89.

Geitmann, A., and Parre, E. (2004). The local cytomechanical properties of growing pollen tubes correspond to the axial distribution of structural cellular elements. Sex. Plant Reprod. **17:** 9–16.

Geitmann, A., and Steer, M.W. (2006). The architecture and properties of the pollen tube cell wall. In The Pollen Tube: A Cellular and Molecular Perspective, Plant Cell Monographs, R. Malhó, ed (Berlin, Heidelberg: Springer Verlag), pp. 177–200.

Goriely, A., and Tabor, M. (2003a). Self-similar tip growth in filamentary organisms. Phys. Rev. Lett. **90:** 1–4.

Goriely, A., and Tabor, M. (2003b). Biomechanical models of hyphal growth in actinomycetes. J. Theor. Biol. **222:** 211–218.

Goriely, A., and Tabor, M. (2008). Mathematical modeling of hyphal tip growth. Fungal Biol. Rev. **22:** 77–83.

Hamant, O., Heisler, M., Jönsson, H., Krupinski, P., Uyttewaaal, M., Bokov, P., Corson, F., Sahlin, P., Boudaoud, A., Meyerowitz, E., Couder, Y., and Traas, J. (2008). Developmental patterning by mechanical signals in *Arabidopsis.* Science **322:** 1650–1655.

Hepler, P.K., Vidali, L., and Cheung, A.Y. (2001). Polarized cell growth in higher plants. Annu. Rev. Cell Dev. Biol. **17:** 159–187.

Hwang, J.-U., Wu, G., Yan, A., Lee, Y.-J., Grierson, C.S., and Yang, Z. (2010). Pollen-tube tip growth requires a balance of lateral propagation and global inhibition of Rho-family GTPase activity. J. Cell Sci. **123:** 340–350.

Kha, H., Tuble, S.C., Kalyanasundaram, S., and Williamson, R.E. (2010). WallGen, software to construct layered cellulose-hemicellulose networks and predict their small deformation mechanics. Plant Physiol. **152:** 774–786.

Klahre, U., Becker, C., Schmitt, A.C., and Kost, B. (2006). Nt-RhoGDI2 regulates Rac/Rop signaling and polar cell growth in tobacco pollen tubes. Plant J. **46:** 1018–1031.

Klahre, U., and Kost, B. (2006). Tobacco RhoGTPase ACTIVATING PROTEIN 1 spatially restricts signaling of RAC/Rop to the apex of pollen tubes. Plant Cell **18:** 3033–3046.

Kost, B., Lemichez, E., Spielhofer, S., Hong, Y., Tolias, K., Carpenter, C., and Chua, N.-H. (1999). Rac homologues and compartmentalized phosphatidylinositol 4, 5-bisphosphate act in a common pathway to regulate polar pollen tube growth. J. Cell Biol. **145:** 317–330.

Kroeger, J.H., Geitmann, A., and Grant, M. (2008). Model for calcium dependent oscillatory growth in pollen tubes. J. Theor. Biol. **253:** 363–374.

Li, Y.-Q., Chen, F., Linskens, H.F., and Cresti, M. (1994). Distribution of unesterified and esterified pectins in cell walls of pollen tubes of flowering plants. Sex. Plant Reprod. **7:** 145–152.

Li, Y.-Q., Faleri, C., Geitmann, A., Zhang, H.Q., and Cresti, M. (1995). Immunogold localization of arabinogalactan proteins, unesterified and esterified pectins in pollen grains and pollen tubes of *Nicotiana tabacum* L. Protoplasma **189:** 26–36.

Lockhart, J.A. (1965). An analysis of irreversible plant cell elongation. J. Theor. Biol. **8:** 264–275.

MacKintosh, F.C., Käs, J., and Janmey, P.A. (1995). Elasticity of semiflexible biopolymer networks. Phys. Rev. Lett. **75:** 4425–4428.

Malhó, R., Read, N.D., Trewavas, A.J., and Salomé Pais, M. (1995). Calcium channel activity during pollen tube growth and reorientation. Plant Cell **7:** 1173–1184.

Mathur, J. (2004). Cell shape development in plants. Trends Plant Sci. **9:** 583–590.

Mathur, J. (2006). Local interactions shape plant cells. Curr. Opin. Cell Biol. **18:** 40–46.

McKenna, S.T., Kunkel, J.G., Bosch, M., Rounds, C.M., Vidali, L., Winship, L.J., and Hepler, P.K. (2009). Exocytosis precedes and predicts the increase in growth in oscillating pollen tubes. Plant Cell **21:** 3026–3040.

O'Kelley, J.C., and Carr, P.H. (1954). An electron micrographic study of the cell walls of elongating cotton fibers, root hairs, and pollen tubes. Am. J. Bot. **41:** 261–264.

Parre, E., and Geitmann, A. (2005a). Pectin and the role of the physical properties of the cell wall in pollen tube growth of *Solanum chacoense.* Planta **220:** 582–592.

Parre, E., and Geitmann, A. (2005b). More than a leak sealant - The physical properties of callose in pollen tubes. Plant Physiol. **137:** 274–286.

Röckel, N., Wolf, S., Kost, B., Rausch, T., and Greiner, S. (2008). Elaborate spatial patterning of cell-wall PME and PMEI at the pollen tube tip involves PMEI endocytosis, and reflects the distribution of esterified and de-esterified pectins. Plant J. **53:** 133–143.

Sassen, M.M.A. (1964). Fine structure of *Petunia* pollen grain and pollen tube. Acta Bot. Neerl. **13:** 175–181.

Schopfer, P. (2006). Biomechanics of plant growth. Am. J. Bot. **93:** 1415–1425.

Smith, L.G., and Oppenheimer, D.G. (2005). Spatial control of cell expansion by the plant cytoskeleton. Annu. Rev. Cell Dev. Biol. **21:** 271–295.

Wang, R., Jiao, Q.-Y., and Wei, D.-Q. (2006). Mechanical response of single plant cells to cell poking: A numerical simulation model. J. Integr. Plant Biol. **48:** 700–705.

Wasteneys, G.O., and Galway, M.E. (2003). Remodeling the cytoskeleton for growth and form: An overview with some new views. Annu. Rev. Plant Biol. **54:** 691–722.

Wilhelm, J., and Frey, E. (2003). Elasticity of stiff polymers. Phys. Rev. Lett. **91:** 108103.

Winship, L.J., Obermeyer, G., Geitmann, A., and Hepler, P.K. (2010). Under pressure, cell walls set the pace. Trends Plant Sci. **15:** 363–369.

Zerzour, R., Kroeger, J.H., and Geitmann, A. (2009). Polar growth in pollen tubes is associated with spatially confined dynamic changes in cell mechanical properties. Dev. Biol. **334:** 437–446.

Zonia, L.E., Müller, M., and Munnik, T. (2006). Hydrodynamics and cell volume oscillations in the pollen tube apical region are integral components of the biomechanics of *Nicotiana tabacum* pollen tube growth. Cell Biochem. Biophys. **46:** 209–232.

Zonia, L., and Munnik, T. (2009). Uncovering hidden treasures in pollen tube growth mechanics. Trends Plant Sci. **14:** 318–327.